

Nonlinear dynamics of electromagnetic field and valley polarization in WSe₂ monolayer

Arqum Hashmi,¹ Shunsuke Yamada,² Atsushi Yamada,² Kazuhiro Yabana,² and Tomohito Otobe^{1, a)}

¹⁾*Kansai Photon Science Institute, National Institutes for Quantum Science and Technology (QST), Kyoto 619-0215, Japan*

²⁾*Center for Computational Sciences, University of Tsukuba, Tsukuba 305-8577, Japan*

(Dated: 2 November 2021)

Linear and nonlinear optical response of WSe₂ monolayer is investigated by two-dimensional Maxwell plus time-dependent density functional theory with spin-orbit interaction. By applying the chiral resonant pulses, the electron dynamics along with high harmonic generation are examined at weak and strong laser fields. WSe₂ monolayer shows the linear optical response at the intensity $I = 10^{10}$ W/cm² while a complex nonlinear behavior is observed at $I = 10^{12}$ W/cm². The nonlinear response of WSe₂ monolayer in terms of saturable absorption is observed at strong laser field. By changing the chirality of the resonant light, a strong circular dichroic effect is observed in the excited state population. A relatively weak laser field shows effective valley polarization while strong field induces spin-polarized carrier peak between $K(K')$ and Γ -point via nonlinear process. On the other hand, the strong laser field shows high harmonics up to the 11th order. Our results demonstrate that circularly polarized resonant pulse generate high harmonics in WSe₂ monolayer of order $3n \pm 1$.

I. INTRODUCTION

Light-matter interaction is a complex phenomenon that is characterized by two different spatial scales, the micrometer scale for the wavelength of the light, and the sub-nanometer scale for the dynamics of electrons¹. The interaction of laser light with solids is a promising tool to investigate the fundamental physical aspects of material properties in condensed matter physics²⁻⁴. In recent days, a tremendous amount of research is focused on the structural, electronic, and optical properties of thin materials^{5,6}. Thin materials of thickness less than the wavelength of light display very attractive electronic and optical properties^{7,8}. In this regard, two-dimensional (2D) layer systems such as graphene^{9,10}, transitional metal dichalcogenides (TMDs)^{11,12}, and phosphorene¹³ are receiving extensive research efforts. Among mentioned 2D materials, TMDs are of particular interest due to broken inversion symmetry and strong spin-orbit coupling (SOC) for valleytronics and spintronics applications. In addition, there is a growing interest to study the nonlinear optical properties of TMDs such as ultrafast carrier dynamics and high order harmonics¹⁴⁻¹⁷.

Time-dependent density-functional theory (TDDFT) has been proposed as a tool to describe the electron dynamics induced by a time-dependent external potential from the first principles¹⁸⁻²⁰. TDDFT has been most successful in the linear response regime to describe electronic excitation^{21,22}. It has also been applied to the nonlinear and nonperturbative dynamics of electrons induced by an intense ultrashort laser pulse²³⁻²⁶. The effectiveness of electron dynamics calculations based on TDDFT is fur-

ther enhanced by combining it with the Maxwell equations for electromagnetic fields of pulsed light²⁷. The combined scheme known as Maxwell-TDDFT formalism has been successfully applied to crystalline solids^{28,29}. The Maxwell-TDDFT scheme is quite comprehensive but a high computational cost limits its applicability. For sufficiently thin materials such as monatomic layers in which macroscopic electromagnetic fields may be treated as spatially uniform within the material, we have developed an efficient approximate method that we call 2D Maxwell-TDDFT scheme^{30,31}. Furthermore, SOC with non-collinear local spin density is incorporated to extend the usefulness of the method to study spin-dependent properties.

In this letter, we study the linear and nonlinear optical response of WSe₂ monolayer by using a circularly polarized driving field. WSe₂ monolayer is chosen to study because of strong SOC and its most promising phenomena of valleytronics. Laser intensity dependence of the valley polarization and light propagation in terms of the transmitted and reflected high harmonics is also investigated by the 2D Maxwell-TDDFT scheme.

II. THEORETICAL FORMALISM

Time-dependent calculations are done using an open-source TDDFT package Scalable Ab initio Light-Matter simulator for Optics and Nanoscience (SALMON). Full details of the SALMON code and its implementation are described elsewhere^{32,33}. Here, we briefly describe the 2D Maxwell-TDDFT method for light propagation in thin layers at normal incidence.

We assume that a thin layer is in the xy plane and a light pulse propagates along the z axis. By using the Maxwell equations, we can describe the propagation of

^{a)}otobe.tomohito@qst.go.jp

the macroscopic electromagnetic fields in the form of the vector potential $\mathbf{A}(z, t)$ as,

$$\left(\frac{1}{c^2} \frac{\partial^2}{\partial t^2} - \frac{\partial^2}{\partial z^2} \right) \mathbf{A}(z, t) = \frac{4\pi}{c} \mathbf{J}(z, t), \quad (1)$$

where $\mathbf{J}(z, t)$ is the macroscopic current density of the thin layer.

For a very thin layer, we may assume the macroscopic electric field inside the thin layer is spatially uniform. We also approximate the macroscopic electric current density in Eq. (1) as

$$\mathbf{J}(z, t) \approx \delta(z) \mathbf{J}_{2D}(t), \quad (2)$$

where $\mathbf{J}_{2D}(t)$ is 2D current density (current per unit area) of the thin layer. We deal with it as a boundary value problem where reflected (transmitted) fields can be determined by the connection conditions at $z = 0$. From Eq. (2), we obtain the continuity equation of $\mathbf{A}(z, t)$ at $z = 0$ as follows

$$\mathbf{A}(z = 0, t) = \mathbf{A}^{(t)}(t) = \mathbf{A}^{(i)}(t) + \mathbf{A}^{(r)}(t), \quad (3)$$

where the $\mathbf{A}^{(i)}$, $\mathbf{A}^{(r)}$, and $\mathbf{A}^{(t)}$ are the incident, reflected, and transmitted fields, respectively. From Eq. (1) and Eq. (2), we get the basic equation of the 2D approximation method,

$$\frac{d\mathbf{A}^{(t)}}{dt} = \frac{d\mathbf{A}^{(i)}}{dt} + 2\pi \mathbf{J}_{2D} [\mathbf{A}^{(t)}] (t). \quad (4)$$

Here, $\mathbf{J}_{2D} [\mathbf{A}^{(t)}] (t)$ is the 2D current density that is determined by the vector potential at $z = 0$ and it is equal to $\mathbf{A}^{(t)}(t)$. Time evolution of electron orbitals in a unit cell of the 2D layer driven by $\mathbf{A}^{(t)}(t)$ is determined by the time-dependent Kohn-Sham (TDKS) equation. By using the velocity gauge, the TDKS equation for the Bloch orbital $u_{b,\mathbf{k}}(\mathbf{r}, t)$ (which is a two-component spinor. b is the band index and \mathbf{k} is the 2D crystal momentum of the thin layer) is described as,

$$i\hbar \frac{\partial}{\partial t} u_{b,\mathbf{k}}(\mathbf{r}, t) = \left[\frac{1}{2m} \left(-i\hbar \nabla + \hbar \mathbf{k} + \frac{e}{c} \mathbf{A}^{(t)}(t) \right)^2 - e\varphi(\mathbf{r}, t) + \hat{v}_{\text{NL}}^{\mathbf{k} + \frac{e}{\hbar c} \mathbf{A}^{(t)}(t)} + v_{\text{xc}}(\mathbf{r}, t) \right] u_{b,\mathbf{k}}(\mathbf{r}, t), \quad (5)$$

where the scalar potential $\varphi(\mathbf{r}, t)$ includes the Hartree potential from the electrons and the local part of the ionic pseudopotentials and we have defined $\hat{v}_{\text{NL}}^{\mathbf{k}} \equiv e^{-i\mathbf{k} \cdot \mathbf{r}} \hat{v}_{\text{NL}} e^{i\mathbf{k} \cdot \mathbf{r}}$. Here, \hat{v}_{NL} and $v_{\text{xc}}(\mathbf{r}, t)$ are the non-local part of the ionic pseudopotentials and exchange-correlation potential, respectively. The SOC is incorporated through the j -dependent nonlocal potential \hat{v}_{NL}^{34} . The Bloch orbitals $u_{b,\mathbf{k}}(\mathbf{r}, t)$ are defined in a box containing the unit cell of the 2D thin layer sandwiched by vacuum regions. The 2D current density $\mathbf{J}_{2D} [\mathbf{A}^{(t)}] (t)$

in Eq. (4) is derived from the Bloch orbitals as follows:

$$\begin{aligned} \mathbf{J}_{2D}(t) = & -\frac{e}{m} \int dz \int_{\Omega} \frac{dx dy}{\Omega} \sum_{b,\mathbf{k}}^{\text{occ}} u_{b,\mathbf{k}}^{\dagger}(\mathbf{r}, t) \\ & \times \left[-i\hbar \nabla + \hbar \mathbf{k} + \frac{e}{c} \mathbf{A}^{(t)}(t) + \frac{m}{i\hbar} \left[\mathbf{r}, \hat{v}_{\text{NL}}^{\mathbf{k} + \frac{e}{\hbar c} \mathbf{A}^{(t)}(t)} \right] \right] u_{b,\mathbf{k}}(\mathbf{r}, t), \end{aligned} \quad (6)$$

where Ω is the area of the 2D unit cell and the sum is taken over the occupied orbitals in the ground state. In the 2D Maxwell-TDDFT method, coupled Eq. (4) and Eq. (5) are simultaneously solved in real time.

In the weak field limit, we can consider a linear response formalism for the 2D approximation method. The constitutive relation in linear response in the form of the 2D current density $\mathbf{J}_{2D} [\mathbf{A}^{(t)}] (t)$ can be described as follows:

$$\begin{aligned} J_{2D,\alpha}(t) = & \sum_{\beta} \int_{-\infty}^t dt' \tilde{\sigma}_{\alpha\beta}(t - t') E_{\beta}^{(t)}(t') \\ = & -\frac{1}{c} \sum_{\beta} \int_{-\infty}^t dt' \tilde{\sigma}_{\alpha\beta}(t - t') \frac{dA_{\beta}^{(t)}(t')}{dt'}, \end{aligned} \quad (7)$$

where α and β are the spatial indices and we have introduced $\tilde{\sigma}_{\alpha\beta}(t - t')$ as the 2D electric conductivity of the thin layer. The frequency-dependent 2D conductivity can be obtained by taking the Fourier transformation of $\tilde{\sigma}_{\alpha\beta}(t)$. For weak field limit, we can simply get the relation between the incident, reflection, and transmission by $\tilde{\sigma}_{\alpha\beta}(\omega)$. For example, for a given incident field $\mathbf{A}^{(i)}(t)$, the transmitted field $\mathbf{A}^{(t)}(t)$ can be constructed by solving the following equation in frequency space, instead of solving Eq. (4) in time.

$$\sum_{\beta} \left(\delta_{\alpha\beta} + \frac{2\pi}{c} \tilde{\sigma}_{\alpha\beta}(\omega) \right) A_{\beta}^{(t)}(\omega) = A_{\alpha}^{(i)}(\omega). \quad (8)$$

WSe₂ monolayer is used to validate our method, Fig. 1(a) illustrates the crystal structure. The lattice constant is set to $a = b = 3.32$ Å. We solve the TDKS equation in the slab geometry with the distance between layers of 20 Å. The dynamics of the 24 (12 electrons for W, and 12 electrons for Se) valence electrons are treated explicitly while the effects of the core electrons are considered through norm-conserving pseudopotentials from the OpenMX library³⁵. The adiabatic local density approximation with Perdew-Zunger functional³⁶ is used for the exchange-correlation. We adopt a spin noncollinear treatment for the exchange-correlation potential^{37,38}. The spatial grid sizes and k-points are optimized according to the convergent results. The determined parameter of the grid size is 0.21 Å while the optimized k-mesh is 15×15 in the 2D Brillouin zone. The time step size is set to 5×10^{-4} femtosecond (fs). We consider the circularly polarized laser field with a time

profile of \cos^4 envelope shape for the vector potential, which gives the electric field of the applied laser pulse through the following equation,

$$\mathbf{A}^{(i)}(t) = -\frac{cE_{\max}}{\omega} \cos^4\left(\pi \frac{t - T_P/2}{T_P}\right) \left[\hat{x} \cos\left\{\omega\left(t - \frac{T_P}{2}\right)\right\} + \hat{y} \sin\left\{\omega\left(t - \frac{T_P}{2}\right)\right\} \right], \quad (0 < t < T_P) \quad (9)$$

where ω is the average frequency, E_{\max} is the maximum amplitude of the electric field and T_P is the pulse duration. We use the frequency of 1.55 eV, and T_P is set to 30 fs and the computation is terminated at 50 fs.

III. RESULTS AND DISCUSSION

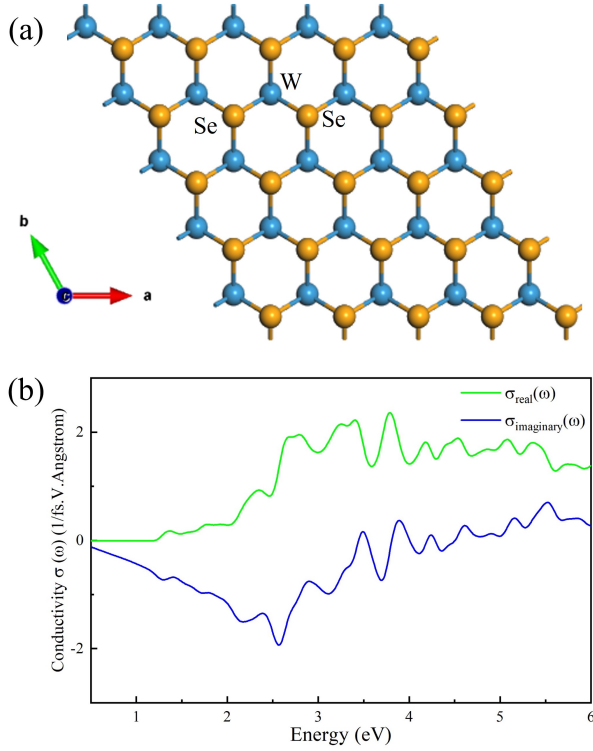


FIG. 1. (a) Crystal structure of WSe₂ in top view. (b) Frequency-dependent optical conductivity of WSe₂ monolayer.

2D WSe₂ monolayer has strong SOC and all the calculations are performed by taking the SOC effect into consideration. The calculated bandgap is ~ 1.25 eV. The Zeeman-type spin splitting due to SOC is also checked. The value of spin splitting for valence band maxima (VBM) is ~ 450 meV, consistent with previous works^{39–41}. Fig. 1(b) depicts the real and imaginary parts of the optical conductivity $\tilde{\sigma}(\omega)$ as a function of the photon energy. $\tilde{\sigma}(\omega)$ provides an understanding of the

band structure properties, the linear dependence of $\tilde{\sigma}(\omega)$ at small energies with zero value at $\omega=0$ reveal the pure semiconducting nature of WSe₂ monolayer. The peaks at higher energies in the optical conductivity correspond to the interband transition from the valence band to the conduction band.

Fig. 2 shows a typical electron dynamics calculation of the WSe₂ monolayer. The time profile of the incident circular polarized electric field and the induced electric current at weak and strong intensity is shown in Fig. 2(a). The current at weak intensity is multiplied by a factor of 10 so that the difference between two currents indicates the nonlinear effect at the strong intensity. For a more clear comparison, we have also shown the X-Y view of the current density in Fig. 2(b). At the weak intensity, the temporal evolution of the induced current mostly follows the driving laser profile, indicating that a linear optical response of WSe₂ monolayer dominates at $I = 10^{10}$ W/cm². We also note that there appears substantial current after the incident pulse ends, since the frequency of the applied laser pulse is above the bandgap value. At the strong intensity, the current is initially very close to the case of the weak intensity. However, the current gradually becomes weaker than that expected from the linear response. We consider that this nonlinear effect suppressing the current comes from the saturable absorption that often appears in various 2D materials^{42–44}. The saturable absorption takes place by two mechanisms: a decrease of electrons in the valence band by the excitation, and an increase of electrons in the conduction band that block the excitation from the valence band. We also note that the current after the incident pulse ends is much weaker than the case of weak intensity. This indicates that nonlinear effect works to cancel the coherence that produced the delayed current in the linear case.

We show the calculated results of electric excitation energy and the number density of excited electrons in Fig. 3. To see the nonlinear effects, we have scaled up the excitation by a factor of 100 for weak intensity. Note that the weak and strong field curves should coincide and show similar behavior if the response is linear. We first consider the case of weak intensity. The electronic excitation energy and the number of excited electrons show a similar time profile with a peak around 18 fs and then decrease. The ratio of the two curves is about 1.8 eV and is close to the photon energy of 1.55 eV, confirming the dominance of the one-photon absorption process. The decrease continues even after the incident pulse ends at 30 fs. This decrease is due to the emission of light that is described in the present 2D Maxwell-TDDFT scheme, and is related to the appearance of the current after the pulse ends in Fig. 2. We next move to the case of strong intensity. The number of excited electrons is much smaller than the estimation by linear excitation mechanism. This is due to the saturable absorption, as we discussed for the current shown in Fig. 2. However, the electronic excitation energy looks to show mostly linear behavior. We consider that this is due to a cancellation of two nonlinear effects,

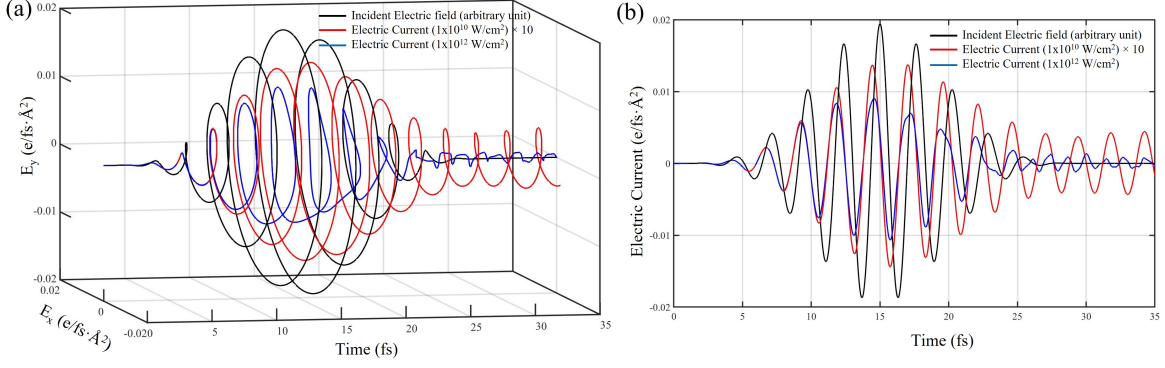


FIG. 2. Typical time evolution calculation for WSe₂ monolayer. (a) Applied electric field waveform and induced electric current density at weak and strong laser field. (b) X-Y view of current density in (a).

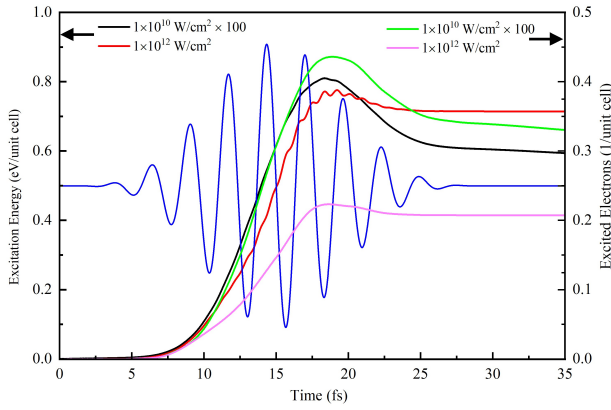


FIG. 3. Temporal development of excitation energies and excited electrons against incident vector potential. For comparison, the results for weak intensity ($I = 10^{10} \text{ W/cm}^2$) is scaled up by a factor of 100.

saturable absorption and multi-photon absorption. Although the number of excited electrons is suppressed by the saturable absorption, the excited electrons can absorb multiple photons, as is evaluated from the ratio of electronic excitation energy and the number of excited electrons which is about 3.8 eV, more than twice of the energy of the incident photon.

To get an understanding of valley pseudospin, we investigate the k-resolved excited electron populations. It is well known that the responses of the conductance for spin-dependent electrons to left- and right-handed resonant circularly polarized light are just the opposite for TMDs^{45–47}. Fig. 4 shows the excited carrier population by right (σ^+) and left (σ^-) circular helicities. Valley polarization results are shown in Fig. 4(a, b) for $I = 10^{10} \text{ W/cm}^2$ and for at $I = 10^{12} \text{ W/cm}^2$ in Fig. 4(c, d). A strong circular dichroic effect is evident in the excited state population both at weak and strong intensity. The valley degeneracy is lifted and pumping with σ^+ polarized light excites electrons in the K valley while

pumping with σ^- polarized light excites the K' valley, so-called valley-spin locking. Due to nonlinear interaction at $I = 10^{12} \text{ W/cm}^2$, the excited electrons are not localized around K/K' and start to spread in the Brillouin zone and a new peak between K (K') and Γ -point appears with nonlinear process. The new peak induced by the strong field may explain the behavior of electric current density at $I = 10^{12} \text{ W/cm}^2$ as shown in Fig. 2. The excited electron at different points of the Brillouin zone indicates the electronic current with different phase and frequency. This phase difference decreases the total current after the pulse ends. Overall, the k-resolved excited electron populations demonstrate that the valley polarization state is quite robust against the field strength.

High harmonic generation (HHG) is a promising tool to study strong-field effects and ultrafast electron dynamics in 2D materials. Experimentally, one can primarily measure the fraction of reflected or transmitted pulses of the light, and the 2D Maxwell-TDDFT scheme used for our calculations can describe the propagation of the light wave dynamics as well. Fig. 5 shows the HHG spectra included the reflected ($\mathbf{A}^{(r)}(t)$) and transmitted ($\mathbf{A}^{(t)}(t)$) pulses. Fig. 5(a) show the HHG spectra for a peak intensity of $I = 10^{10} \text{ W/cm}^2$ while Fig. 5(b) is for $I = 10^{12} \text{ W/cm}^2$. First of all, HHG spectra of the reflected and transmitted pulses completely coincide with each other except for the fundamental frequency, as is understood from the continuity equation of Eq. (3). We find that a resonant circularly polarized driver ($\omega = 1.55 \text{ eV}$) generates strong high harmonics. For the weak intensity of 10^{10} W/cm^2 , the spectrum includes very weak HHG components except for the second harmonic. It was as expected because the electronic current density shows the linear optical response at this intensity. On the other hand, the strong intensity of 10^{12} W/cm^2 (Fig. 5(b)) shows the harmonic order up to 11th order. WSe₂ monolayer displays both odd and even harmonic peaks. Our results show that the in-plane harmonics of WSe₂ monolayer under resonant circular driver has an order of $3n \pm 1$ (where n is an integer), while the multiple of 3 har-

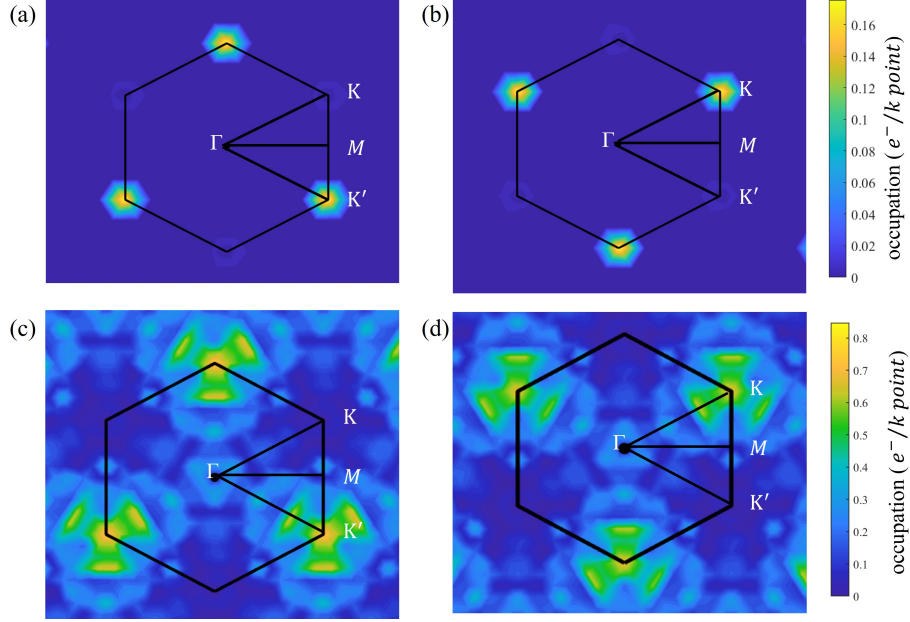


FIG. 4. Distribution of k-resolved electron populations in the first BZ of the conduction band at the end of the pulse (a) Right hand and (b) Left hand circularly polarized light at $I = 10^{10}$ W/cm². (c, d) Same as the upper panel but at $I = 10^{12}$ W/cm. Electron population is summed over the entire conduction band

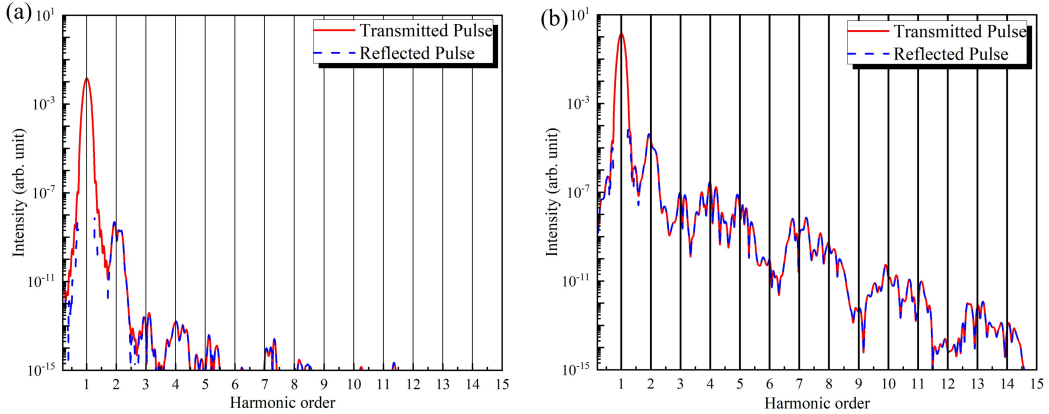


FIG. 5. HHG spectra of WSe₂ monolayer. High harmonic signals of the reflected and the transmitted wave at (a) $I = 10^{10}$ W/cm² (b) $I = 10^{12}$ W/cm².

monic orders are suppressed. The three-fold rotational symmetry of the WSe₂ monolayer lead to the selection rule of $3n \pm 1$. The 3rd harmonic appears in Fig. 5(b) is the exception to this rule and it may be related to the relative phase effect as explained in Ref.⁴⁸.

IV. CONCLUSION

In this work, we have studied the linear and nonlinear optical response of WSe₂ monolayer by the classical Maxwell equations combined with TDKS equations to describe the propagation of electromagnetic fields in thin 2D layers. By applying the chiral resonant pulses,

the electron dynamics and HHG are shown at a weak and strong laser field. WSe₂ monolayer shows the linear optical response at weak intensity. By changing the chirality of the resonant light, a strong circular dichroic effect is observed in the excited state population. A relatively weak laser field shows effective valley polarization while strong field induces new peak of spin-polarized carrier by nonlinear process. WSe₂ monolayer displays the nonlinear optical characteristic of saturable absorption at strong laser field. The 2D Maxwell-TDDFT scheme offers a clear advantage to measure the HHG in terms of the transmitted and reflected waves. HHG spectra of the reflected and transmitted pulses completely coincide with each other. HHG in WSe₂ monolayer is observed up

to the 11th order and circularly polarized resonant driver have high harmonics of $3n \pm 1$ order in WSe₂ monolayer.

V. AUTHOR INFORMATION

Corresponding Author

*E-mail: otobe.tomohito@qst.go.jp

Author Contributions

Notes

The authors declare no competing financial interest.

VI. ACKNOWLEDGMENT

This research is supported by JST-CREST under Grant No. JP-MJCR16N5. This research is also partially supported by JSPS KAKENHI Grant No. 20H02649, and MEXT Quantum Leap Flagship Program (MEXT Q-LEAP) under Grant No. JPMXS0118068681 and JPMXS0118067246. The numerical calculations are carried out using the computer facilities of the Fugaku through the HPCI System Research Project (Project ID: hp210137), SGI8600 at Japan Atomic Energy Agency (JAEA), and Multidisciplinary Cooperative Research Program in CCS, University of Tsukuba.

- ¹Hertzog, M., Wang, M., Mony, J. & Börjesson, K. Strong light-matter interactions: a new direction within chemistry. *Chemical Society Reviews* **48**, 937–961 (2019).
- ²Armstrong, J., Bloembergen, N., Ducuing, J. & Pershan, P. S. Interactions between light waves in a nonlinear dielectric. *Physical review* **127**, 1918 (1962).
- ³Fox, M. Optical properties of solids (2002).
- ⁴Dressel, M. & Grüner, G. Electrodynamics of solids: optical properties of electrons in matter (2002).
- ⁵Novoselov, K. S. et al. Two-dimensional atomic crystals. *Proceedings of the National Academy of Sciences* **102**, 10451–10453 (2005).
- ⁶Tan, T., Jiang, X., Wang, C., Yao, B. & Zhang, H. 2d material optoelectronics for information functional device applications: status and challenges. *Advanced Science* **7**, 2000058 (2020).
- ⁷Britnell, L. et al. Strong light-matter interactions in heterostructures of atomically thin films. *Science* **340**, 1311–1314 (2013).
- ⁸Kats, M. A. & Capasso, F. Optical absorbers based on strong interference in ultra-thin films. *Laser & Photonics Reviews* **10**, 735–749 (2016).
- ⁹Novoselov, K. S. et al. Electric field effect in atomically thin carbon films. *science* **306**, 666–669 (2004).
- ¹⁰Novoselov, K. S. et al. A roadmap for graphene. *nature* **490**, 192–200 (2012).
- ¹¹Wang, Q. H., Kalantar-Zadeh, K., Kis, A., Coleman, J. N. & Strano, M. S. Electronics and optoelectronics of two-dimensional transition metal dichalcogenides. *Nature nanotechnology* **7**, 699–712 (2012).
- ¹²Chhowalla, M. et al. The chemistry of two-dimensional layered transition metal dichalcogenide nanosheets. *Nature chemistry* **5**, 263–275 (2013).
- ¹³Xia, F., Wang, H. & Jia, Y. Rediscovering black phosphorus as an anisotropic layered material for optoelectronics and electronics. *Nature communications* **5**, 1–6 (2014).
- ¹⁴Autere, A. et al. Nonlinear optics with 2d layered materials. *Advanced Materials* **30**, 1705963 (2018).
- ¹⁵Langer, F. et al. Lightwave valleytronics in a monolayer of tungsten diselenide. *Nature* **557**, 76–80 (2018).
- ¹⁶Liu, H. et al. High-harmonic generation from an atomically thin semiconductor. *Nature Physics* **13**, 262–265 (2017).
- ¹⁷Säynätjoki, A. et al. Ultra-strong nonlinear optical processes and trigonal warping in mos 2 layers. *Nature communications* **8**, 1–8 (2017).
- ¹⁸Runge, E. & Gross, E. K. Density-functional theory for time-dependent systems. *Physical Review Letters* **52**, 997 (1984).
- ¹⁹Yabana, K. & Bertsch, G. Time-dependent local-density approximation in real time. *Physical Review B* **54**, 4484 (1996).
- ²⁰Ullrich, C. A. *Time-dependent density-functional theory: concepts and applications* (OUP Oxford, 2011).
- ²¹Yabana, K., Nakatsukasa, T., Iwata, J.-I. & Bertsch, G. Real-time, real-space implementation of the linear response time-dependent density-functional theory. *physica status solidi (b)* **243**, 1121–1138 (2006).
- ²²Laurent, A. D. & Jacquemin, D. Td-dft benchmarks: a review. *International Journal of Quantum Chemistry* **113**, 2019–2039 (2013).
- ²³Nobusada, K. & Yabana, K. High-order harmonic generation from silver clusters: Laser-frequency dependence and the screening effect of d electrons. *Physical Review A* **70**, 043411 (2004).
- ²⁴Castro, A., Marques, M. A., Alonso, J. A., Bertsch, G. F. & Rubio, A. Excited states dynamics in time-dependent density functional theory. *The European Physical Journal D-Atomic, Molecular, Optical and Plasma Physics* **28**, 211–218 (2004).
- ²⁵Otobe, T. et al. First-principles electron dynamics simulation for optical breakdown of dielectrics under an intense laser field. *Physical Review B* **77**, 165104 (2008).
- ²⁶Shinohara, Y. et al. Coherent phonon generation in time-dependent density functional theory. *Physical Review B* **82**, 155110 (2010).
- ²⁷Yabana, K., Sugiyama, T., Shinohara, Y., Otobe, T. & Bertsch, G. Time-dependent density functional theory for strong electromagnetic fields in crystalline solids. *Physical Review B* **85**, 045134 (2012).
- ²⁸Lee, K.-M. et al. First-principles simulation of the optical response of bulk and thin-film α -quartz irradiated with an ultra-short intense laser pulse. *Journal of Applied Physics* **115**, 053519 (2014).
- ²⁹Sato, S. et al. Time-dependent density functional theory of high-intensity short-pulse laser irradiation on insulators. *Physical Review B* **92**, 205413 (2015).
- ³⁰Yamada, S., Noda, M., Nobusada, K. & Yabana, K. Time-dependent density functional theory for interaction of ultrashort light pulse with thin materials. *Physical Review B* **98**, 245147 (2018).
- ³¹Yamada, S. & Yabana, K. Determining the optimum thickness for high harmonic generation from nanoscale thin films: An ab initio computational study. *Physical Review B* **103**, 155426 (2021).
- ³²Noda, M. et al. Salmon: Scalable ab-initio light-matter simulator for optics and nanoscience. *Computer Physics Communications* **235**, 356–365 (2019).
- ³³Salmon official. <http://salmon-tddft.jp>.
- ³⁴Theurich, G. & Hill, N. A. Self-consistent treatment of spin-orbit coupling in solids using relativistic fully separable ab initio pseudopotentials. *Physical Review B* **64**, 073106 (2001).
- ³⁵Morrison, I., Bylander, D. & Kleinman, L. Nonlocal hermitian norm-conserving vanderbilt pseudopotential. *Physical Review B* **47**, 6728 (1993).
- ³⁶Perdew, J. P. & Wang, Y. Accurate and simple analytic representation of the electron-gas correlation energy. *Physical review B* **45**, 13244 (1992).
- ³⁷Von Barth, U. & Hedin, L. A local exchange-correlation potential for the spin polarized case. i. *Journal of Physics C: Solid State Physics* **5**, 1629 (1972).
- ³⁸Oda, T., Pasquarello, A. & Car, R. Fully unconstrained approach to noncollinear magnetism: application to small fe clusters. *Physical review letters* **80**, 3622 (1998).

- ³⁹Kormányos, A. et al. k·p theory for two-dimensional transition metal dichalcogenide semiconductors. *2D Materials* **2**, 022001 (2015).
- ⁴⁰Rasmussen, F. A. & Thygesen, K. S. Computational 2d materials database: electronic structure of transition-metal dichalcogenides and oxides. *The Journal of Physical Chemistry C* **119**, 13169–13183 (2015).
- ⁴¹Le, D. et al. Spin-orbit coupling in the band structure of monolayer wse₂. *Journal of Physics: Condensed Matter* **27**, 182201 (2015).
- ⁴²Wang, K. et al. Ultrafast saturable absorption of two-dimensional mos₂ nanosheets. *ACS nano* **7**, 9260–9267 (2013).
- ⁴³Liu, M., Liu, W., Liu, X., Wang, Y. & Wei, Z. Application of transition metal dichalcogenides in mid-infrared fiber laser. *Nano Select* **2**, 37–46 (2021).
- ⁴⁴Uemoto, M., Kurata, S., Kawaguchi, N. & Yabana, K. First-principles study of ultrafast and nonlinear optical properties of graphite thin films. *Physical Review B* **103**, 085433 (2021).
- ⁴⁵Zaumseil, J. Electronic control of circularly polarized light emission. *Science* **344**, 702–703 (2014).
- ⁴⁶Zhang, Y., Oka, T., Suzuki, R., Ye, J. & Iwasa, Y. Electrically switchable chiral light-emitting transistor. *Science* **344**, 725–728 (2014).
- ⁴⁷Xie, L. & Cui, X. Manipulating spin-polarized photocurrents in 2d transition metal dichalcogenides. *Proceedings of the National Academy of Sciences* **113**, 3746–3750 (2016).
- ⁴⁸Alon, O. E., Averbukh, V. & Moiseyev, N. Selection rules for the high harmonic generation spectra. *Physical review letters* **80**, 3743 (1998).